sustainability

Article

Coupling Global Parameters and Local Flow Optimization of a Pulsed Ejector for Proton Exchange Membrane Fuel Cells

Chao Li [1], Baigang Sun [1,2] and Lingzhi Bao [1,*]

[1] School of Mechanical Engineering, Beijing Institute of Technology, Beijing 100081, China; elwenlc@bit.edu.cn (C.L.); sunbg@bit.edu.cn (B.S.)
[2] Beijing Institute of Technology Chongqing Innovation Center, Beijing Institute of Technology, Chongqing 401120, China
* Correspondence: lingzhibao@bit.edu.cn

Abstract: Proton exchange membrane fuel cells (PEMFCs), as an important utilization of hydrogen energy, contribute to the sustainable development of global energy. Pulsed ejectors have a high potential for improving the hydrogen utilization of PEMFCs in the full operating range by circulating unconsumed hydrogen. In this study, a pulsed ejector applied to a 120 kW fuel cell was designed, and the flow characteristics were analysed using computational fluid dynamics (CFD). Based on the data from the CFD model, the global optimization of the ejector was carried out using the Gaussian process regression (GPR) surrogate model and the grey wolf optimization (GWO) algorithm. The local structure was then further optimized using an adjoint method coupling streamlining modification that takes into account the local flow characteristics. The CFD results showed that, under a fixed structure, increasing the pressure difference between the secondary flow and the ejector outlet would promote boundary layer separation, shorten the shockwave chain length, change the effective flow area of the secondary flow, and lower the entrainment ratio (ER). The analytical results from the GPR model indicated significant interactions among the structural parameters. The globally optimized ejector using GPR and GWO improved the hydrogen entrainment ratio from 1.42 to 3.12 at the design point. Furthermore, the results of streamlining local optimization show that the entrainment ratio increased by 1.67% at the design point and increased by up to 3.99% over the full operating range compared to the optimized ejector by global optimization.

Keywords: PEMFC; pulsed ejector; local flow; gaussian process regression; global optimization; adjoint method

check for updates

Citation: Li, C.; Sun, B.; Bao, L. Coupling Global Parameters and Local Flow Optimization of a Pulsed Ejector for Proton Exchange Membrane Fuel Cells. *Sustainability* **2024**, *16*, 4170. https://doi.org/10.3390/su16104170

Academic Editor: Paride Gullo

Received: 16 April 2024
Revised: 14 May 2024
Accepted: 14 May 2024
Published: 16 May 2024

1. Introduction

Hydrogen energy is a renewable energy carrier and plays an important role in the sustainable development of global energy. PEMFCs are clean and efficient energy conversion devices using hydrogen and are considered to be the next generation of power units [1]. During the operation of a PEMFC system, excess hydrogen is supplied to ensure dynamic output performance; the unconsumed hydrogen needs to be recirculated by a hydrogen-recirculating device. Hydrogen recirculation can not only mitigate hydrogen starvation of the fuel cell but also prevent the accumulation of liquid water in the anode and reduce hydrogen emissions to improve environmental sustainability [2]. At present, there are primarily two types of hydrogen-recirculating devices: mechanical pumps and ejectors. The mechanical pumps—driven by motors—not only require extra fuel cell stack net power but also have several issues, such as friction, leakage, and oil pollution [3–5]. In comparison to mechanical pumps, ejectors have the advantages of a simple structure, stable operation, high reliability, and low power consumption. Therefore, they are ideal devices for hydrogen recirculation in PEMFCs [6].

The ejectors used in fuel cells can be divided into continuous and pulsed types. The mass flow rate of a continuous ejector is controlled by changing the hydrogen supply pressure or nozzle area. The pulsed ejector facilitates the pulsed control of the flow rate by intermittently opening and closing the injector. The working principle and geometry of the hydrogen recirculation ejector are illustrated in Figure 1. High-pressure hydrogen from the hydrogen tank, called primary flow, enters the nozzle from the pressure regulator. The exhaust gas of the PEMFC anode, called secondary flow, is entrained under viscous shear. The two flows are then mixed in a mixing chamber with momentum and energy exchange. Finally, the mixed gas is pressurized in a diffuser and supplied to the stack.

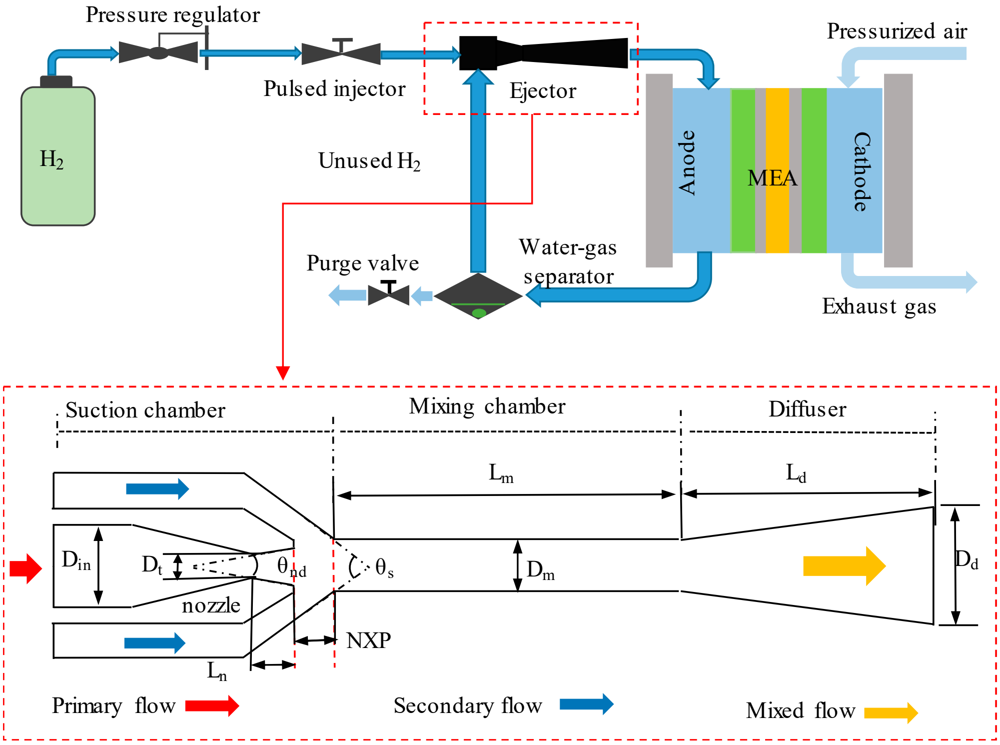

Figure 1. Schematic of PEMFC anode recirculation system based on ejectors.

Recently, several studies have been carried out to improve the performance of continuous ejectors. Further, it is known that the structural parameters and operating conditions have an important effect on the entrainment ratio [7–12]. Pei et al. [13] used the dynamic pressure drop boundary in the CFD model to optimize the nozzle diameter, the mixing chamber diameter, the mixing chamber length, and the nozzle exit position, respectively. Wang et al. [14] performed single-factor optimization of the diffuser angle and mixing chamber diameter. Yin et al. [9] implemented a sequential method to optimize the structural parameters, which was a combination of single-round optimization and multi-round optimization. Maghsoodi et al. [15] used 167 CFD results to train their neural network model, combining it with the genetic algorithm and bat algorithm to optimize the nozzle outlet location, mixing chamber length, diffuser length, and angle. They obtained highly consistent results from the two optimization algorithms, which were better than the single-round optimization of factors. Similar to Maghsoodi's research, Bai et al. [16] used the hybrid artificial fish swarm optimization algorithm to optimize the ejector. Zhang et al. [17] studied the optimization of the nozzle outlet position under different working fluid pressures and different ejector fluid pressures and fitted the optimal nozzle outlet position formula for the design of the self-regulating ejector. Yang et al. [18] used a new pressure drop model to analyse the sensitivity of parameters such as the nozzle diameter, mixing chamber diameter, nozzle outlet distance, mixer length, diffuser length, and diffuser angle and optimized the ejector, considering the interactions between the two parameters. Yan et al. [19] optimized structural parameters with six different sequences, finding that single-round optimization cannot achieve global optimization. The number of rounds depends on the optimization order and varies with the operating conditions. Wu et al. [20] conducted a single-factor analysis and multi-factor analysis of parameters such as the diameter of the nozzle outlet, nozzle exit position, and the diameter of the nozzle contraction section. Amin et al. [21] trained a kriging surrogate model and adopted the factorial method to optimize the geometry of natural gas ejectors. The entrainment ratio reached 19.45% at the design point. Bian et al. [22] carried out single-round optimization on the mixing chamber diameter, nozzle outlet position, and mixing chamber length of the fuel cell ejector, considering the effect of boundary layer separation. Ringstad et al. [23] used the CFD dataset to train the GPR machine learning model, and a gradient descent method was adopted to optimize the structural parameters and operating conditions of the CO_2 ejector. In addition, some optimizations based on theoretical [24,25] and analytical models [26] have also been studied in PEMFCs. They calculated parameters for a few key internal cross-sections through extensive simplification and assumptions, such as velocity distribution functions. Meanwhile, internal losses of ejectors are characterized by coefficients, and these models cannot provide internal flow characteristics. Therefore, CFD models can provide the most comprehensive ejector characteristics for flow behaviour-based optimization, including global-scale and local-scale characteristics.

The operation of ejectors is particularly challenging due to the dynamic operation of the PEMFC system. For continuous ejectors controlled by variable pressures, performance cannot be guaranteed at low PEMFC currents. As a result, some ejector schemes have been investigated in PEMFCs for a wide operating range. Brunner et al. [27] proposed a variable flow rate ejector controlled by a moving needle and successfully applied it to a 17 kW fuel cell system. Wang et al. [28–30] and Han et al. [31] used multi-nozzle ejectors in the anode recirculation system of the PEMFC, which effectively expanded the operating range of the hydrogen-recirculating units. Han et al. [11] and Yu et al. [32] proposed bypass-ejector devices to improve the entrained performance of high-power conditions and widen the operating range of PEMFCs. Kim et al. [33] developed a dual-ejector anode recirculating unit that could be used in the wider working range required for PEMFC systems than a fixed single ejector. Huang et al. [34] also proposed a dual-ejector scheme, including a high-flow ejector and a low-flow ejector, and verified it through a system-level model. Further, the pulsed ejector is also an effective way to improve performance under all operating conditions. To cover a wider range of stack power, Hwang et al. [35] controlled an ejector to circulate unused hydrogen using a hybrid control scheme, which combines the continuous hydrogen supply mode and pulsed hydrogen supply mode. The pulsed hydrogen supply mode is used when the stack power is less than the ejector operating range. Jung et al. [4] designed an ejector-based hydrogen supply system consisting of an ejector and a proportional valve, using a pulsed hydrogen supply to overcome the ejector's performance limitations under low-power conditions. Singer et al. [36] proposed a design toolchain for a pulsed injector–ejector unit, including basic calculation, 1D ejector calculation, 1D anode system simulation, CFD flow analysis, and experimental verification. However, they did conduct detailed optimization.

In summary, the structural parameters significantly affect the performance of hydrogen ejectors, and the optimal design methods have been widely studied. However, there is relatively little research on the optimization of ejectors that consider both global parameters and local flow behaviour simultaneously. Although the pulsed ejector concept has been mentioned in fuel cell systems, the optimization of pulsed ejectors has not been studied systematically to date. Therefore, the aim of this study is to propose an optimization strategy to improve the performance of the pulsed ejector considering both global and local flow optimization. In Section 2, the operating characteristics of the pulsed ejector in PEMFCs are analysed, and a CFD model of the ejector is developed. In Section 3, the internal flow characteristics and the entrainment performance under different secondary inlet pressures and pressure differences are studied, followed by a discussion of the interactive relationships among different structural parameters based on the trained Gaussian process regression model. Then, the grey wolf optimization algorithm is utilized to carry out the global optimization of the pulsed ejector. Finally, the local structure of the pulsed ejector is optimized using the adjoint method coupling streamlining modification to improve the ejector performance, and the performance improvement is validated under different operating conditions.

2. Methodology

Herein, a PEMFC pulsed ejector was designed for high-power stack and full operating conditions. The process of design and optimization is essential for improving the performance of the ejector. The proposed optimization procedure for the pulsed ejector is as follows:

First, the operating conditions of the design points were selected according to the operational requirements of the reactor and the characteristics of the pulsed ejector. Second, the original structural parameters of the pulsed ejector were designed using 1D thermodynamics, aerodynamics, and relevant empirical formulas [37]. Third, a high-precision prediction model was constructed within a certain range. The input parameters are the structural parameters, and the output is the entrainment ratio. Sampling was carried out within a certain range; the high-precision model was trained based on machine learning principles, and the intelligent algorithm was used for global optimization. In this paper, Gaussian process regression (GPR) [23] was used for prediction, and grey wolf optimization (GWO) [38] was used to optimize the kernel function to improve the predictive accuracy of the model. Global optimization was also performed using GWO. The optimization results were checked to ensure that the optimal structural parameters lie in the middle of the sampling range or meet the design and manufacturing limitations. If this condition was not met, the sampling range needed to be adjusted. Finally, the local shape sensitivity of the optimized ejector obtained through global optimization was analysed, and local flow optimization was carried out using the adjoint method until the optimization objective was completely convergent, completing the optimization process of the ejector. The proposed optimization strategy is shown in Figure 2.

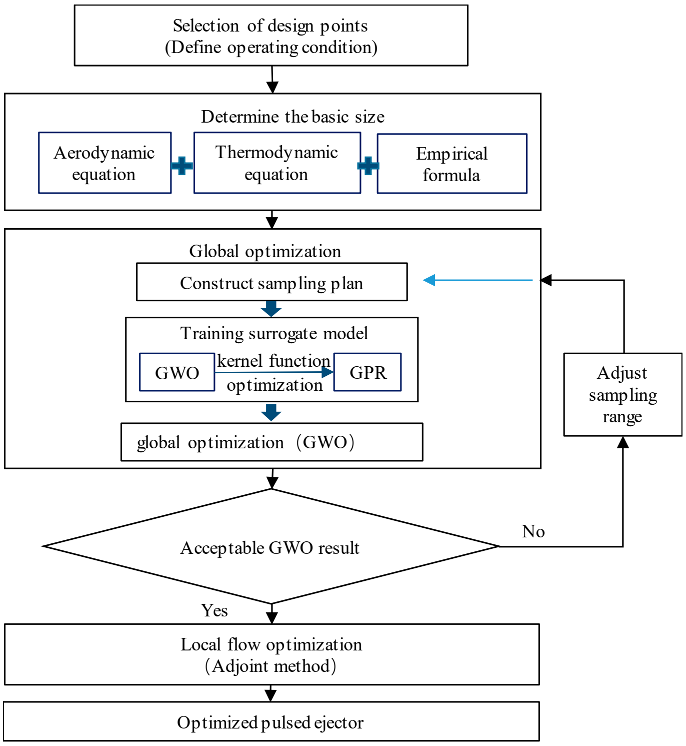

Figure 2. Design flowchart of the optimization strategy.

2.1. Characteristics of the Pulsed Ejector in PEMFCs

A pulsed ejector in a PEMFC operates on a pulsed cycle, where the injector is turned on for a period of time and then turned off. Figure 3 shows the operating characteristics of such an ejector. During the opening phase of the injector, the inlet pressure of the stack increases, while the outlet pressure of the stack first decreases and then increases. When the injector is turned on, the pressure difference between the inlet and outlet of the stack is relatively small, and the entrainment ratio increases rapidly and then decreases, resulting in an excessive secondary flow rate entrained into the stack supply manifold. As the opening time increases, the pressure difference between the inlet and outlet gradually increases. This results in a decrease in the entrained flow rate and an increase in the stack anode exhaust gas. Thus, the return manifold pressure begins to increase. During the pulse shut-off phase, the stack supply manifold pressure drops because there is no flow supply in the supply manifold. At the same time, the return manifold pressure continues to rise. Because of the pressure difference, the stack continues to vent into the exhaust manifold, and no gas is recirculated to the stack supply manifold. The supply manifold pressure drops rapidly and gradually approaches the exhaust manifold pressure after the solenoid has been closed for some time.

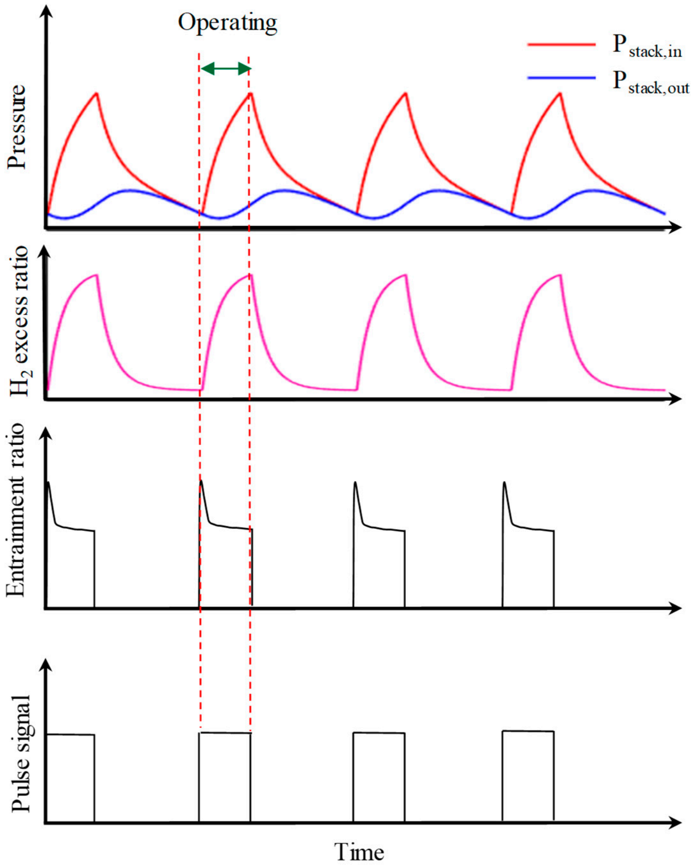

Figure 3. Operating characteristic of the PEMFC anode recirculation system based on the pulsed ejector.

As shown in Figure 3, the hydrogen excess ratio is related to the pressure difference between the supply and exhaust manifold. The operating characteristics of the pulsed ejector-based stack provide boundary conditions for the pulsed ejector design. Therefore, the primary flow pressure can be considered to be constant when the solenoid is in the opening phase, while the secondary flow pressure and back pressure are always changing during a pulse cycle.

2.2. Structural Parameters and Operating Conditions

In this paper, the pulsed ejector was applied to a 120 kW PEMFC stack. The maximum nozzle pressure was 15 bar, and the diameter of the nozzle was a key parameter. Considering the purge process, the purge flow rate was assumed to be 20% of the required flow rate of the maximum current. Therefore, the maximum primary mass flow rate of the pulsed ejector can be calculated using the following formula [22]:

$$m_{in} = 1.2m_{com} = \frac{NI_{\max}}{2F}M_{H_2}, \tag{1}$$

where m_{in} presents the maximum primary mass flow rate of the pulsed ejector, m_{com} presents the mass flow rate of hydrogen consumed by the fuel cell stack, N is the cell number of the stack, $I_{\max}$ is the maximum current, M_{H_2} is the molar weight of hydrogen, and F is the Faraday constant.

The nozzle diameter can be calculated according to the following formula [28]:

$$D_t = \sqrt{\frac{4m_{in}c_{cr}}{P_p\gamma\nu_{cr}\pi}}, \tag{2}$$

$$\nu_{cr} = (\frac{2}{\gamma+1})^{\gamma/(\gamma-1)}, \tag{3}$$

and

$$c_{cr} = (\frac{2\gamma}{\gamma+1}R_pT_p)^{1/2}, \tag{4}$$

where ν_{cr} is the critical pressure ratio, c_{cr} is the critical velocity of the gas, P_p is the primary flow pressure, T_p is the primary flow temperature, R_p is the gas constant of the primary flow, and γ is the gas-specific heat ratio.

Other structural parameters shown in Figure 1 are calculated using empirical formulas [37]. The original structural parameters of the pulsed ejector are presented in Table 1. The performance of the pulsed ejector was evaluated through the entrainment ratio, which is defined as

$$ER = \frac{m_s}{m_p}, \tag{5}$$

where m_p is the primary flow mass rate, and m_s is the secondary flow mass rate.

Table 1. Geometric parameters of the original pulsed ejector.

Parameters	Symbol	Value
Nozzle inlet diameter	D_{in}	10 mm
Nozzle throat diameter	D_t	1.8 mm
Nozzle diffuse angle	θ_{nd}	6°
Length of nozzle	L_{nd}	6 mm
Nozzle exit position	NXP	7 mm
Suction angle	θ_s	60°
Mixing chamber diameter	D_m	7 mm
Length of mixing chamber	L_m	25 mm
Diffuser angle	θ_d	5°
Diffuser exit diameter	D_d	21 mm

According to the analysis in Section 2.1, changes in the pressure difference and secondary flow pressure will lead to significant changes in an ejector's performance. In the 120 kW PEMFC stack used in this research, the actual pressure drop of the stack under the maximum current is less than 10 kPa at the rated excess ratio, as presented in Table 2.

Table 2. Operating conditions of a 120 kW PEMFC.

Power	Current Density	Pin	Excess Ratio	Pressure Difference
17 kW	0.2 A/cm^2	1.4 bar	3	3.0 kPa
48 kW	0.6 A/cm^2	1.6 bar	1.7	3.9 kPa
76 kW	1.0 A/cm^2	1.8 bar	1.5	5.6 kPa
100 kW	1.4 A/cm^2	2.0 bar	1.5	7.2 kPa
120 kW	1.8 A/cm^2	2.2 bar	1.5	8.8 kPa

However, a larger excess ratio is considered after the application of the pulsed ejector; the operating conditions of the pulsed ejector are presented in Table 3. Cases 1–5 represent the simulated operating conditions when varying the ejector exit pressure during the pulse period at a constant current. Cases 5–9 represent the simulated operating conditions when varying the ejector secondary flow pressure at different currents. Finally, case 5 was selected as the design point.

Table 3. Operating conditions of the pulsed ejector.

Case	P_p	T_p	P_s	T_s	P_e
1~5	15 bar	298 K	2 bar	70 °C	2~2.2 bar (interval 0.05 bar)
5~9	-	-	2~1.2 bar (interval 0.2 bar)	-	P_s + 0.2 bar

2.3. Numerical Model

In order to study the performance of the ejector, some important assumptions are introduced to establish the CFD model. According to the description in Section 2.1, the ejector operates under relatively stable conditions most of the time during the pulse period, and the flow inside the ejector is assumed to be compressible and stable. Since the pressure inside the ejector is not too high, it can be assumed to be an ideal gas. Additionally, ignoring the influence of gravity, the working gas is considered a single-phase flow. And the wall is assumed to be an adiabatic wall. Turbulence models have a significant impact on the entrainment ratio and flow patterns in ejectors. Several researchers have compared different turbulence models used in ejectors, and they have proven that the SST k–ω turbulence model can achieve accurate prediction of ejector characteristics in both global performance and local flow characteristics [39,40]. So, the SST k–ω turbulence model is selected in the next studies. Based on the above assumptions and model selection, the flow control equations and turbulence equations can be found in the literature [11]. The detailed model settings are shown in Table 4.

A structured mesh grid was adopted in this research, created in ICEM, as shown in Figure 4a. The near-wall mesh was refined to y^+ close to 1 to capture the flow change of the boundary layer, as shown in Figure 4b. A grid-independent study was performed to improve the accuracy of the simulation. Furthermore, five levels of the grid are compared, namely a coarse mesh with 45,207 cells, a coarser mesh with 91,245 cells, a medium mesh with 142,648 cells, a fine mesh with 252,902 cells, and a finer mesh with 362,902 cells.

Table 4. The detailed model settings.

Simulation	Setting
Platform	Ansys Fluent
Viscous model	k-ω *SST* Viscous Heating, Compressibility Effects
Material Properties	Density: ideal gas Specific heat: piecewise polynomial Thermal conductivity: polynomial Viscosity: sutherland
Boundary	Primary inlet: pressure inlet (pulsed ejector On) Secondary inlet: pressure inlet Ejector outlet: pressure outlet
Solver	Pressure-based coupled solver
Discretization	Second-order scheme
Convergence criterion	Residuals less than 10^{-6}

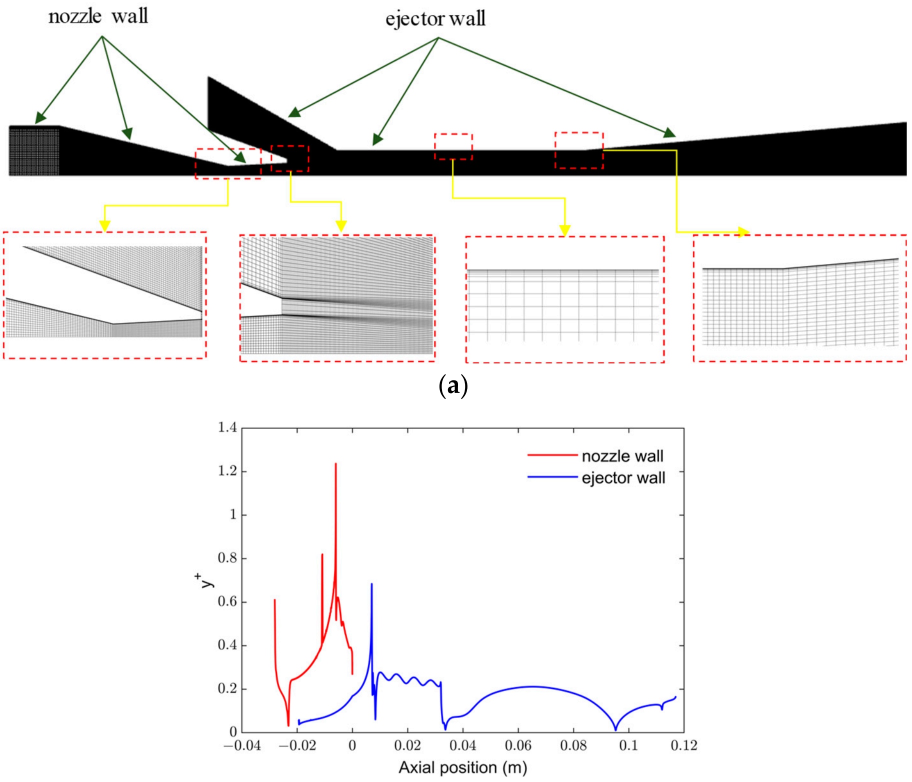

(**a**)

(**b**)

Figure 4. Mesh of the computational domain. (**a**) Grid division. (**b**) y^+ of Wall.

The grid independence was verified using both the entrainment ratio and the central Mach number. Entrainment ratios under different grid levels are compared in Table 5, which shows that the relative deviation of the entrainment ratio was lower than 1% when the cell number was above 91,254. Figure 5 shows the diversification of the centre flow Mach number under different grid levels to verify the internal flow characteristics. The Mach number was found to be approximately constant in all locations when the cell number exceeded 142,648. Therefore, the medium mesh level was selected for subsequent calculation research in this work.

To validate the CFD model, an air ejector was utilized for calculations and compared with experimental data from Chong's research [41]. The primary flow pressure is 1 MPa, and the secondary flow pressure is 0.5 MPa, while the ejector outlet pressure varies from 0.4 to 0.7 MPa. Entrainment ratio comparisons between the CFD model and the experimental results are shown in Figure 6a. It was found that the simulated entrainment ratios are highly consistent with the experimental data in terms of changing trends. From the perspective of the entrainment ratio, there is a deviation between the CFD results and the experimental values. The possible reason is that the viscous shear characteristic in the turbulence model is over-predicted. At low back pressures, the development of the viscous shear layer reduces the flow area of the secondary flow, resulting in a lower calculated secondary flow rate. At high back pressures, the primary flow core is suppressed, and the flow rate of the secondary flow is overestimated with greater viscous shear force. In addition, the simulated results of different wall static pressures are compared in Figure 6b. The deviations of the wall static pressure were no more than 10%, most of which were within 5%. Therefore, the model established in this study can predict the characteristics of the hydrogen ejector accurately.

Table 5. Grid independence verification results of the entrainment ratio.

Grid Size	Cell Number	ER	Relative Deviation
Coarse mesh	45,207	1.4155	-
Coarser mesh	91,254	1.4315	1.13%
Medium mesh	142,648	1.4362	0.33%
Fine mesh	252,902	1.4393	0.22%
Finer mesh	362,902	1.4384	0.06%

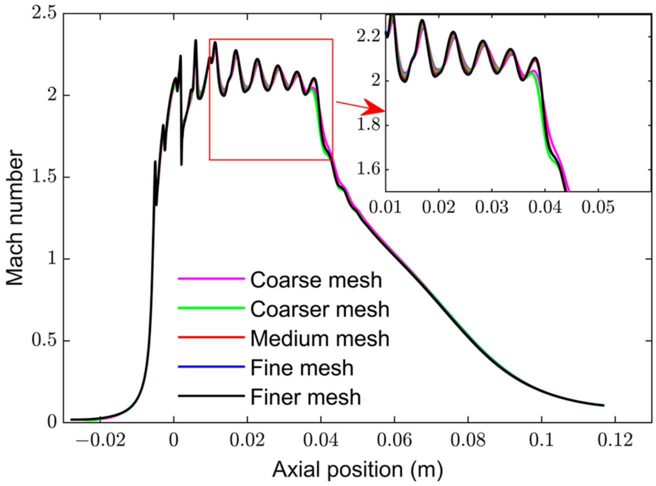

Figure 5. Central Mach number at different mesh levels.

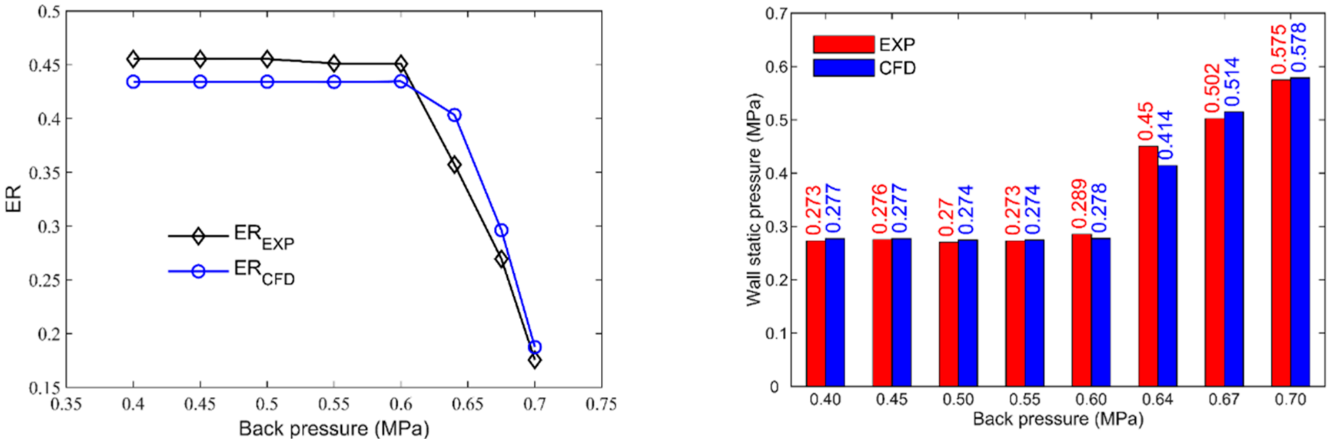

(**a**) (**b**)

Figure 6. Comparison of simulation results and experimental data [41]. (**a**) Entrainment ratio. (**b**) Wall static pressure.

2.4. Gaussian Process Regression

GPR is a potential machine learning algorithm that is used for supervised learning tasks, such as regression and classification. It is based on the concept of modelling the interactive relationship between input and output variables, which is based on the assumption that the unknown function values are drawn from a Gaussian process. The Gaussian process is the underlying function that generates the output values [23].

The goal of GPR is to learn a function that maps the input variables to the output variables. The input–output function for GPR is typically written as

$$y(x) = f(X) + \varepsilon. \tag{6}$$

The function of a Gaussian process can be written as

$$f(X) = GP(m(X), K(X, X')), \tag{7}$$

where $m(X)$ is a mean function, and $K(X, X')$ is a covariance function.

The error term or the noise term in the input–output function Equation (6) can be written as

$$\varepsilon = \sigma_n^2 I. \tag{8}$$

In Equation (7), $m(X)$ represents the average value of the function at each point in the input space, while $K(X, X')$ represents the degree of similarity between different points in the input space. In this research, the covariance function is referred to as a combined kernel function, which includes a radial basis function kernel and a white noise kernel. It can be written as follows:

$$\Sigma = K(X, X') + \sigma_n^2 I \tag{9}$$

and

$$K(X, X') = \sigma_y^2 \exp(-\frac{\|X - X'\|^2}{2\ell^2}), \tag{10}$$

where X is the matrix of n input vectors, I is an identity matrix, ℓ is a hyperparameter known as the length scale, σ_y is a hyperparameter known as the signal standard deviation, and σ_n is a hyperparameter known as the standard deviation of the noise.

In GPR, hyperparameters $[\ell, \sigma_y, \sigma_n]$ control the behaviour and accuracy of the algorithm. Therefore, the hyperparameters of the combined kernel function should be optimized to train more accurate models in this research. During training, the GPR algorithm estimates the parameters of the mean and covariance functions using the training data. Once the parameters are estimated, the GPR model can be used to predict the output values for new input values.

2.5. Adjoint Method

The adjoint method in Fluent is a technique used for calculating the sensitivity derivatives of a given objective function with respect to the structural variables in a computational fluid dynamics (CFD) simulation. It works by computing the gradient of the objective function with respect to the structural variables using backward integration of the adjoint equation. These equations are obtained by taking derivatives of the governing equations of fluid flow with respect to the objective functions.

The adjoint equations are solved simultaneously with the forward equations describing the fluid flow. This facilitates the efficient computation of the sensitivity derivatives, as it requires only one additional simulation with the adjoint equations, instead of multiple simulations for each structural variable. Once the sensitivity derivatives are computed, they can be used to optimize the structure of the fluid device by adjusting the structural variables in a way that maximizes or minimizes the objective function. This can be conducted using gradient-based optimization techniques, such as gradient descent or quasi-Newton methods.

3. Results and Discussion

3.1. Influence of the Operating Conditions

3.1.1. Influence of the Pressure Difference

Figure 7 shows the influence of the back pressure on the entrainment ratio when the primary flow pressure is 15 bar and the secondary flow pressure is 2 bar. The performance curve of a typical ejector is shown in Figure 7a; when the back pressure is less than the critical back pressure (2 bar), the Mach line (red line) is in contact with the wall of the mixing chamber (black line), as shown in Figure 7c. This means that both the primary flow and the secondary flow are choked. The velocity of the secondary flow at a certain position in the mixing chamber is higher than the local sonic speed, and the entrainment ratio remains constant at 1.55, which is called the critical mode. When the back pressure is more than the critical back pressure, the ejector operates in the subcritical mode. Further, the entrainment ratio decreases with increases in the back pressure. In the subcritical mode, the primary flow is choked, and the secondary flow Mach number is less than 1. This is the main operating range for ejectors in PEMFCs. When the back pressure reaches the breakdown point (3.087 bar), the entrainment ratio drops to 0. When the back pressure is higher than the breakdown point, the ejector cannot entrain the secondary flow. In the back-flow mode, the secondary flow's mass flow rate is negative, and the secondary inlet becomes an outlet. Therefore, to stop the ejector from operating in the back-flow mode in fuel cells, a check valve or on–off valve is usually installed at the secondary inlet.

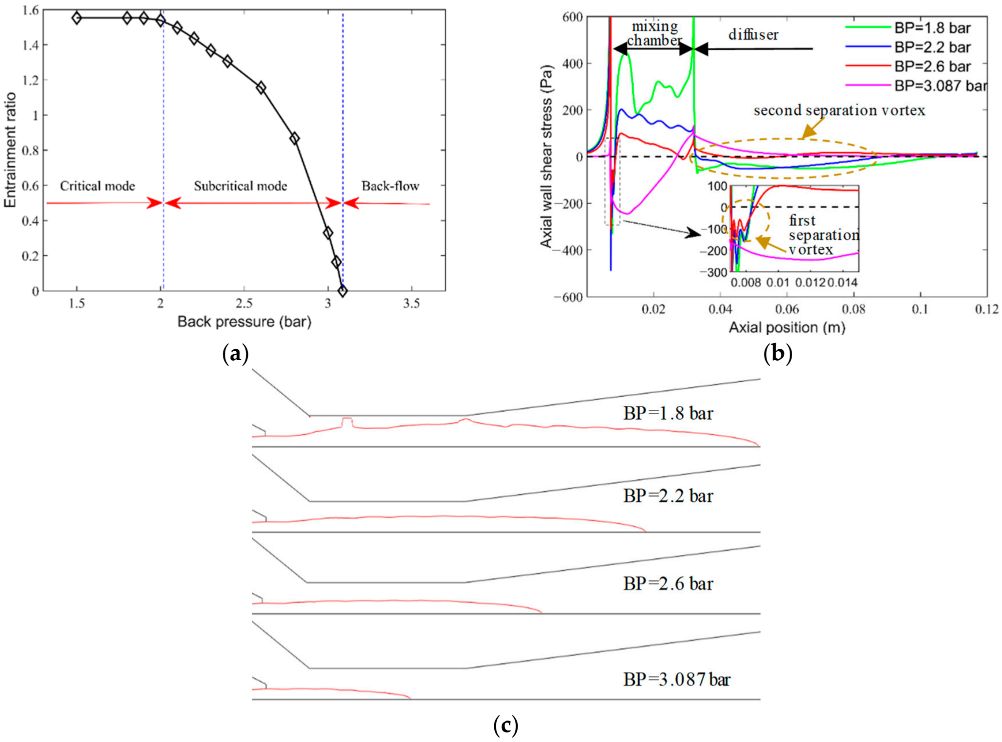

(**a**) (**b**)

(**c**)

Figure 7. Influence of back pressure on the ejector characteristics. (**a**) Entrainment ratio. (**b**) Axial wall shear stress. (**c**) Mach line.

Figure 7b compares the axial shear stress under different back pressures. It can be seen that a separation vortex is generated at the entrance of the mixing chamber. This phenomenon is caused by the direction change of secondary flow under high-speed flows, which is related to the angle of the suction chamber. In this study, the suction chamber angle of the original ejector is selected based on an empirical formula [37]; the structure has not been optimized sufficiently, making this phenomenon more obvious. This separation vortex is called the first separation vortex in the rest of the paper. After the first separation vortex, due to the combined action of the pressure difference, velocity, and wall viscosity, a second separation vortex will be generated in the mixing chamber or diffuser. In the critical mode, the wall shear stress in the mixing chamber is higher because the flow velocity in the mixing chamber is higher, and the viscous shear action with the wall is enhanced. In the subcritical mode, with the back pressure increasing from 2.2 bar to 2.6 bar, the first separation vortex size at the entrance of the mixing chamber increases, and the axial wall shear stress in the mixing chamber gradually decreases. At the breakdown point, because the separation vortex at the entrance of the mixing chamber occupies most of the mixing chamber area (other than the primary flow area), the secondary flow mass rate will be 0. Figure 7c compares the Mach line of Mt = 1. It can be seen that the increase in the back pressure reduces the velocity and momentum from the primary flow, so the shear effect on the secondary flow becomes weaker, and the entrainment ratio decreases.

Figure 8 shows the ejector's performance curve at different pressure differences when the primary flow pressure is 15 bar and the ejector outlet pressure is 2.2 bar. The variation trend of the entrainment ratio in Figure 8a is similar to that for the subcritical mode in Figure 7. As the pressure difference gradually increases, the scale of the first separation vortex becomes larger, and the position of the second separation vortex gradually moves from the diffuser to the mixing chamber, as shown in Figure 8b. Figure 8c shows that the velocity of the primary flow in the mixing chamber decreases; the momentum exchange of the primary flow to the secondary flow is weakened due to viscous shear. Under the force of the outlet back pressure, the back force against the flow is increased, and a vortex is generated in the mixing chamber. As a result, the flow area of the secondary flow decreases, along with the entrainment ratio.

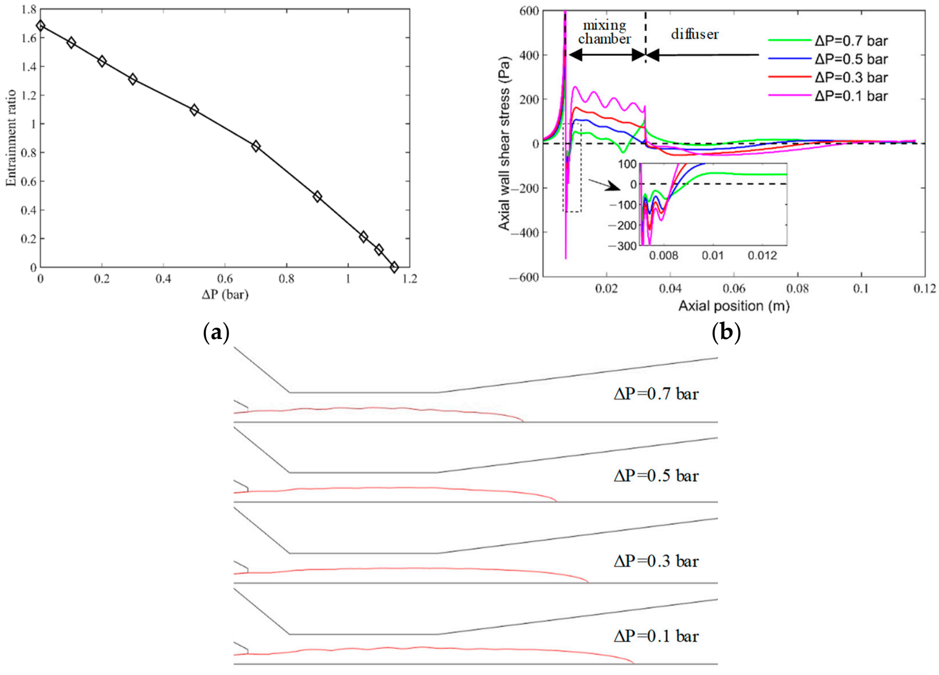

(**a**) (**b**)

(**c**)

Figure 8. Influence of the pressure difference on the ejector characteristics. (**a**) Entrainment ratio. (**b**) Axial wall pressure. (**c**) Mach line.

3.1.2. Influence of Secondary Flow Pressure

Figure 9 shows the influence of different secondary inlet pressures when the primary flow pressure is 15 bar and the differential pressure is fixed at 0.2 bar. It can be seen in Figure 9a that the entrainment ratio gradually increases from 0.86 to 1.55 when the secondary flow pressure increases from 1.2 bar to 2.2 bar. An interesting phenomenon is evident in Figure 9b, where the average axial wall shear stress in the mixed chamber remains basically constant but fluctuates greatly when the secondary flow pressure is small. From Figure 9c, it can be seen that the central Mach number decreases as the secondary flow pressure increases, which is a result of the Bernoulli effect. Further, the entrainment ratio increases; it could be interpreted that, although the velocity reduces, the corresponding pressure ratio also reduces, resulting in a decrease in the energy required for entraining the secondary flow. Moreover, it can be seen from Figure 9d that the wall static pressure in the mixed chamber fluctuates less when the secondary flow pressure increases from 1.4 bar to 2.0 bar. The internal flow is more uniform, and the flow loss is smaller. It can be considered that, in the case of the same pressure difference, the increase in the secondary pressure is beneficial to promoting the uniformity of the flow in the mixing chamber and reducing the momentum dissipation of the mixing fluid.

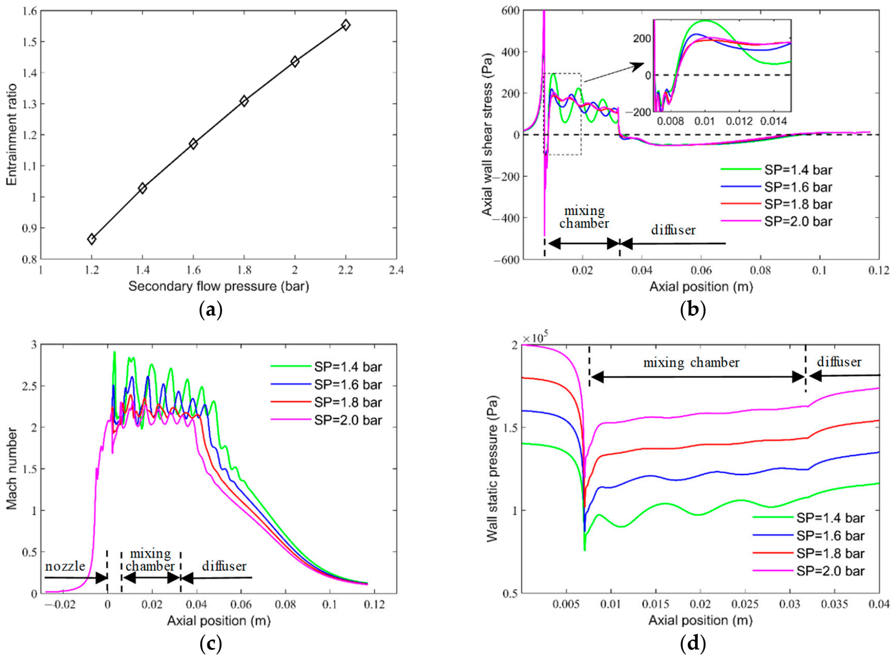

(a) (b) (c) (d)

Figure 9. Influence of the secondary flow pressure on the ejector characteristics. (**a**) Entrainment ratio. (**b**) Axial wall shear stress. (**c**) Central Mach number. (**d**) Wall pressure.

3.2. Analysis of the Gaussian Process Regression

3.2.1. Gaussian Process Regression Model

In this study, considering the computational cycle problem, only four key structural parameters (D_m, NXP, L_m, and θ_{nd}) are selected for global optimization based on our previous research [42]. To obtain the dataset for training the GPR model, the sampling range is initially determined, and the sampling range is adjusted according to the calculation results. The final sampling range is $D_m \in$ [6 mm, 14 mm], $NXP \in$ [5 mm, 35 mm], $L_m \in$ [15 mm, 45 mm], and $\theta_{nd} \in$ [0°, 20°]. To ensure that the training is accurate, 300 sampling points were selected using the Latin hypercube sampling method. Here, 85% of the data points were used for model training, and 15% were used for model testing.

The prediction accuracy of GPR is closely related to the kernel function. Therefore, the three hyperparameters (signal standard deviation, characteristic length scale, and noise standard deviation) involved in the GPR kernel function in this paper are optimized using the grey wolf algorithm. The grey wolf optimizer is a metaheuristic algorithm that is inspired by the social hierarchy and hunting behaviour of grey wolves in the wild. The objective function is the root mean square error of the test set. Figure 10 shows the scattering point distribution of the predicted response value and the CFD simulation value of the test set. The results show that most of the GPR predicted values are sufficiently close to the CFD results. The maximum deviation between the predicted value and CFD value is 0.1, and the maximum relative error is 4.2%, which falls within the acceptable range. This indicates that the GPR model trained in this paper has the ability to provide sufficiently accurate prediction data.

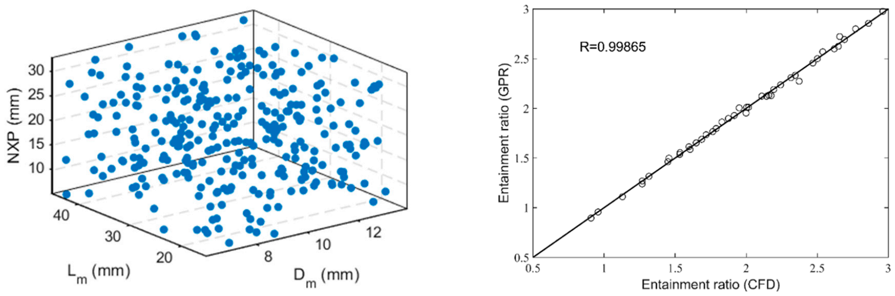

(**a**) (**b**)

Figure 10. GPR prediction model. (**a**) Latin hypercube sampling space. (**b**) Comparisons of CFD results and GPR predicted values.

3.2.2. Interactions of the Structural Parameters

In this study, the Sobol method is introduced to perform global sensitivity analysis to evaluate the importance of different structural parameters on the ejector performance. This analysis helps to elucidate input–output relationships and multivariate interactions between input parameters. At the same time, based on the results of global sensitivity analysis, more reasonable parameter analysis can be performed. The first-order Sobol index reflects the univariate influence of individual input parameters on the output variance, while the total Sobol index represents the contribution of both individual and interactive input parameters. In this paper, individuals with a total Sobol index greater than 0.1 are defined as sensitive parameters and paired combinations with a second-order Sobol index greater than 0.02 are defined as having an interaction relationship. In addition, the differences between first-order and total Sobol indices are more remarkable, which highlights the higher-order interactions with other sensitive parameters.

As shown in Figure 11a, the entrainment ratio exhibits strong sensitivity to those structural parameters. The sensitive structural parameters of the entrainment ratio in the pulsed ejector are D_m, L_m, and NXP. It means that optimizing D_m is a reliable way to maximize the entrainment ratio cause its first-order Sobol index of 0.6 is much greater than other parameters. From the perspective of the total Sobol index, the contribution of different structural parameters to the total variance is relatively complex. Among them, D_m has the most significant effect, with a total Sobol index of 0.725. The sensitivity to θ_{nd} is relatively low, with a total Sobol index of 0.05. At the same time, the difference between the first-order index and the total index is more significant, which highlights the interaction effect between each parameter. As shown in Figure 11b, the contribution of the interaction between the two parameters represented by the second-order exponential is plotted as a 3D histogram. The pairwise interactions of θ_{nd} and other parameters show relatively small effects, with a lower second-order index (<0.004). The other three parameters show some pairwise interactions on the entrainment ratio. The similar pairwise interactions between D_m, L_m, and NXP indicate that there is a strong coupling relationship among these three parameters. It suggests that optimizing these three parameters simultaneously is more efficient in maximizing ejector performance.

Figure 12a shows that at a certain D_m value, increases in L_m increase the entrainment ratio. This is because increasing L_m improves the mixing time and space of the primary flow and the secondary flow, making the flow velocity of the mixed fluid entering the diffuser more uniform and avoiding the formation of a separation vortex in the diffuser, which would reduce the pressure recovery ability. Figure 12b shows the interactions between NXP and θ_{nd}. When the NXP increases from 0 mm to 30 mm, the θ_{nd} corresponding to the optimal entrainment ratio decreases from 10° to 6°. However, the rate of change of the NXP is steeper than that of θ_{nd}. Figure 12c shows that the optimal D_m increases first and then decreases under certain NXP values. This is because when D_m is small, the effective flow area of the secondary flow is small, and the entrained capacity is limited. When D_m is large, the back force increases, leading to the formation of local separation vortexes. Figure 12d shows that both NXP and L_m could influence the entrainment ratio of the pulsed ejector, and the sensitivity of NXP is higher than that of L_m. Figure 12e shows that the sensitivity of L_m and θnd to the entrainment ratio is relatively small, while the sensitivity of Lm is higher than that of θ_{nd}. Figure 12f shows that the optimal θ_{nd} increases first and then decreases. When θ_{nd} is small, the primary flow is in an under-expansion state at the nozzle outlet. Since the airflow is not sufficiently accelerated, the irreversible loss caused by expansion increases when it leaves the nozzle, so the entrained ability is weakened. When θ_{nd} is larger, the primary flow is in a state of excessive expansion, leading to circulation at the nozzle, and the velocity is reduced when contacting the secondary flow, reducing the entrained ability. Based on the abovementioned analysis, it can be seen that the four key structural parameters have a coupled relationship with the entrainment ratio.

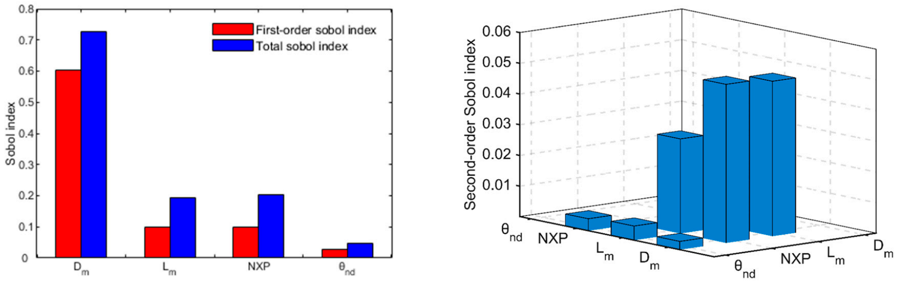

(**a**) (**b**)

Figure 11. Sensitivity analysis. (**a**) First-order and total Sobol index. (**b**) Second-order Sobol index.

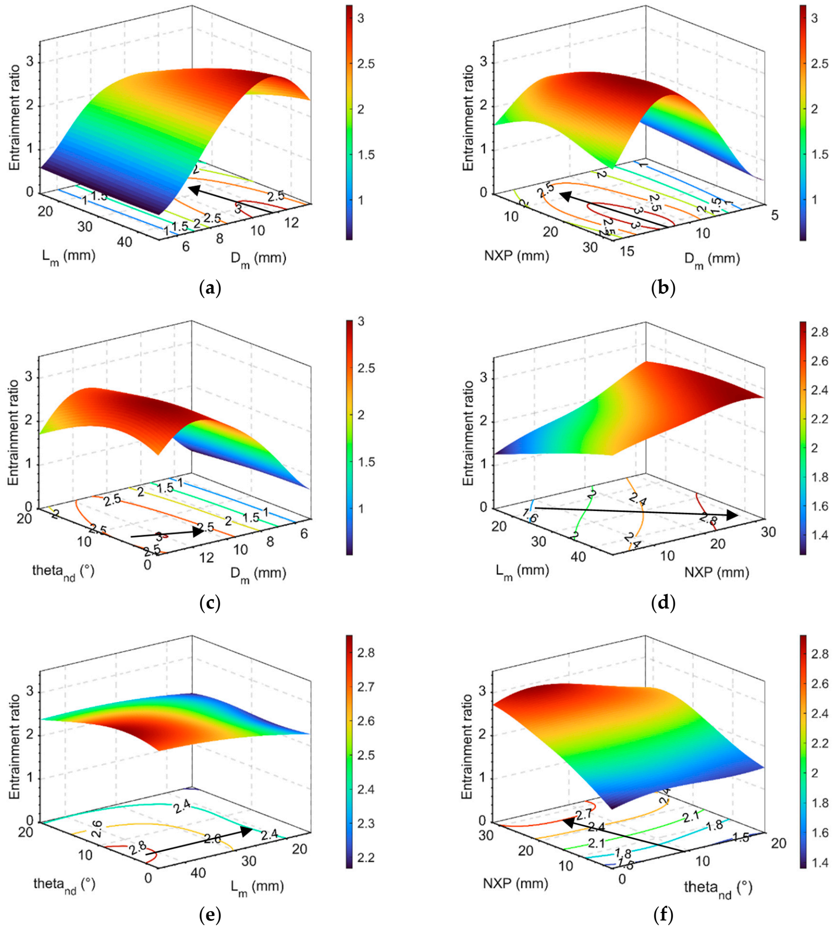

(**a**) (**b**) (**c**) (**d**) (**e**) (**f**)

Figure 12. Interactions of other parameters. (**a**) D_m and L_m. (**b**) D_m and NXP. (**c**) D_m and θ_{nd}. (**d**) NXP and L_m. (**e**) L_m and θ_{nd}. (**f**) θ_{nd} and NXP.

3.3. Global Optimization

The negative ER is used as the optimization objective, and the maximum ER is solved using the grey wolf optimization algorithm. Generally, a larger number of wolves leads to better exploration of the search space; thus, the number of wolves is set to 100, and the maximum number of iterations to 200. After 53 iterations, the fitness function converges. The optimized GWO ejector parameters are an 11.59 mm mixing cavity diameter, 45 mm mixing cavity length, 25.58 mm nozzle exit position, and 6.54° nozzle diffusion angle. The highest entrainment ratio is 3.12.

The GPR globally optimized ejector was verified via CFD, and the entrainment ratio was calculated to be 3.12; the deviation from the GPR model prediction was 0.1%, and the optimized entrainment ratio was 117.6% higher than that of the original ejector, as shown in Table 6. The internal flow is as shown in Figure 13; the nozzle of the original ejector is too close to the entrance of the mixing chamber. To ensure full mixing, the diameter of the mixing chamber is small, and the circulation area of the effective secondary flow is small. In the optimized ejector, the high-speed primary flow fully contacts the secondary flow in the suction chamber and entrains the secondary flow to the exit due to the effect of viscous shear. There are two separation vortexes in the original ejector, as shown in Figure 13a. The first separation vortex is located at the entrance of the mixing chamber, and the vortex size is 1.20 mm. The second separation vortex is generated in the diffuser, and the vortex size is 56.14 mm. This is because the length of the mixing chamber is too small; Figure 13b shows an extremely uneven velocity distribution at the mixing chamber outlet of the original ejector, and the separation vortex is generated under the action of the pressure gradient and the viscosity near the wall. After optimization, the separation vortex only appears at the entrance of the mixing chamber due to the angle of the suction chamber (namely, θ_s in Figure 1); the scale is 0.98 mm, and the minimum axial wall shear stress is −271 Pa. Therefore, the secondary flow rate of the optimized ejector increases.

Table 6. Performance comparisons of the original ejector and optimized ejector via GPR.

Optimized Ejector	ER	Min Axial Wall Shear Stress (Pa)	Max Axial Wall Shear Stress (Pa)	Vortex Scale (mm)
Original	1.43	−487	1632	First vortex: 1.20 Second vortex: 56.14
Optimized ejector via GPR	3.12	−271	936	0.98

3.4. Local Flow Optimization

3.4.1. Sensitivity of the Local Shape

In the local flow optimization process, the mass flow rate of the secondary flow is selected as the optimization objective. First, the flow region of the ejector optimized via GPR is evaluated. Figure 14 shows the structural sensitivity, which is predicted before optimization to determine the region to be optimized. It can be seen from Figure 14 that the nozzle region and the local structure at the entrance of the mixing chamber are sensitive to the target. Due to the small size of the nozzle, manufacturing accuracy should be considered during the optimization of the nozzle. Therefore, this paper selects the entrance of the mixing chamber for optimization.

3.4.2. Optimization Performance Analysis

The shape of the entrance of the mixing chamber was optimized using the adjoint method first. In the adjoint optimization process, 20 iterations were set along with optimization, and performance convergence was achieved in the fifth iteration. Then, the streamlining structure is carried out based on the results of adjoint optimization. Figure 15a compares the structure of the ejector before and after optimization. The junction region between the mixing chamber and the suction chamber is optimized. The entrainment ratio increased from 3.12 to 3.17 after adjoint optimization, and the entrainment ratio rose to

3.18 after streamlining optimization. The angle of the junction area is reduced, and the entrainment ratio is improved. Therefore, it is recommended to set a transition structure in this region when designing ejectors, using a small suction chamber angle or streamlined suction chamber.

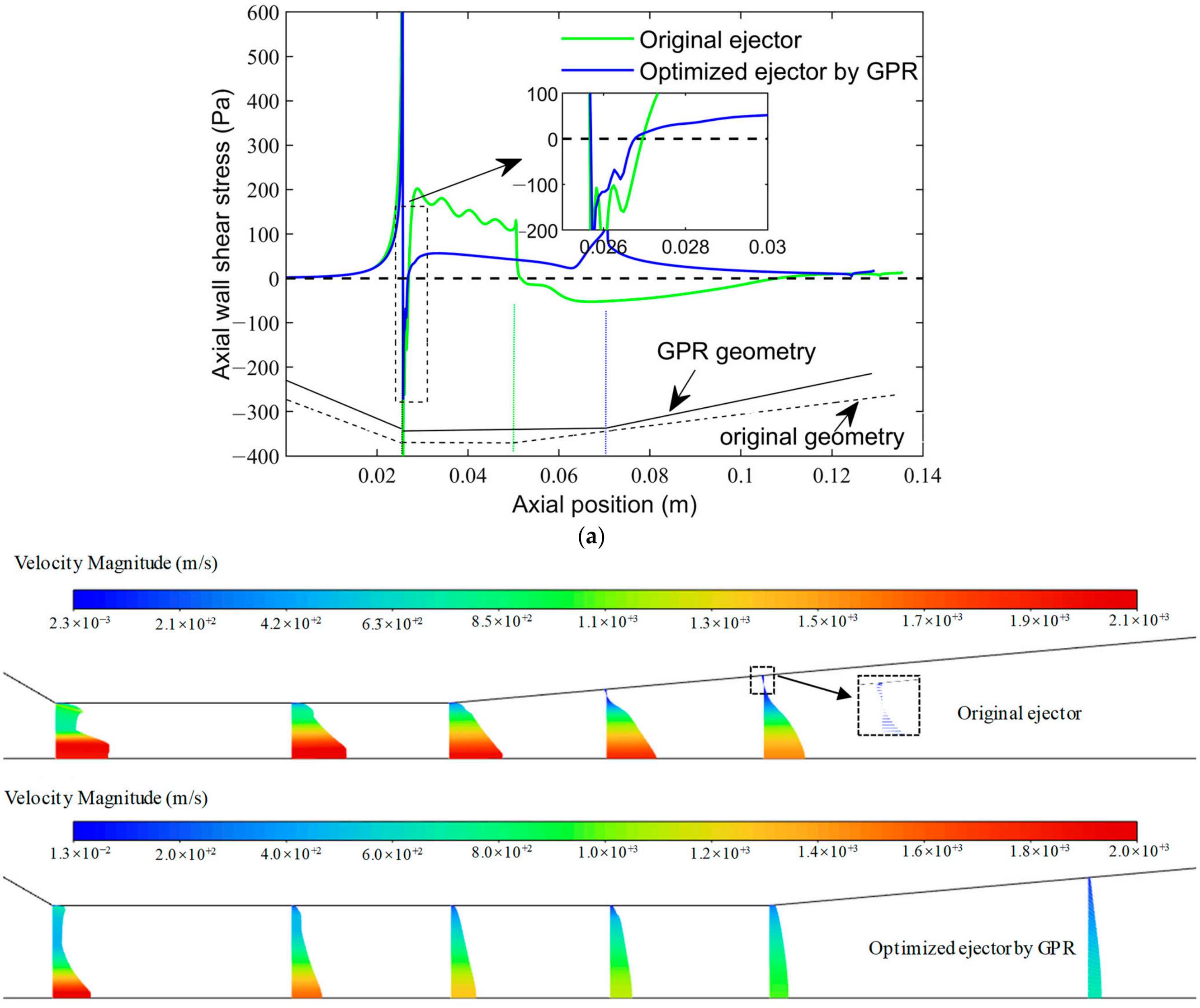

(**a**)

(**b**)

Figure 13. Flow characteristic comparison of the original ejector and ejector optimized via GPR. (**a**) Axial wall shear stress. (**b**) Velocity distribution.

The internal mechanism of the increased entrainment ratio can be understood using the internal flow. Figure 15 also compares the central Mach number and wall axial static pressure of the three ejectors. It can be seen in Figure 15b that the separation vortex of the optimized ejector-based local flow, both adjoint and streamlining modification, is significantly reduced at the entrance of the mixing chamber. The results are shown in Table 7, where it can be seen that there is a separation vortex at the entrance of the mixing chamber, and the size of the vortex is reduced from 0.98 mm to 0 mm with the optimized streamlining ejector. The minimum axial wall shear stress increased from −271 Pa to 53 Pa. The decrease in the central Mach number means that the flow in the mixing chamber is more uniform in Figure 15c, and the energy and momentum of the primary flow are fully transferred to the secondary flow. Therefore, the secondary flow rate increases after optimization using the adjoint method.

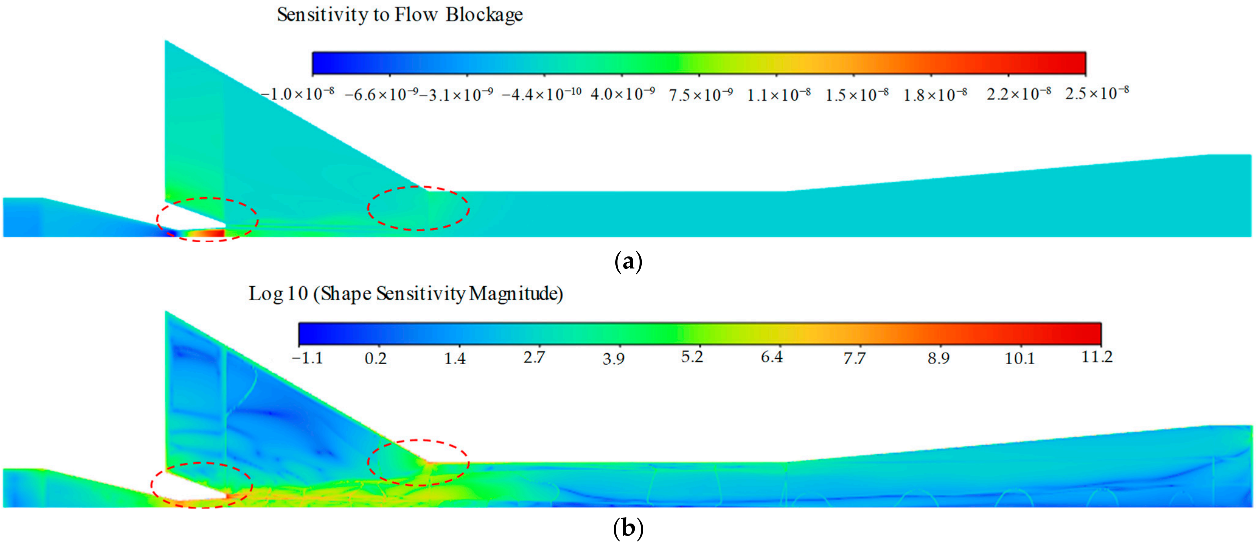

Figure 14. Sensitivity of the local structure. (**a**) Sensitivity to flow blockage. (**b**) Shape sensitivity.

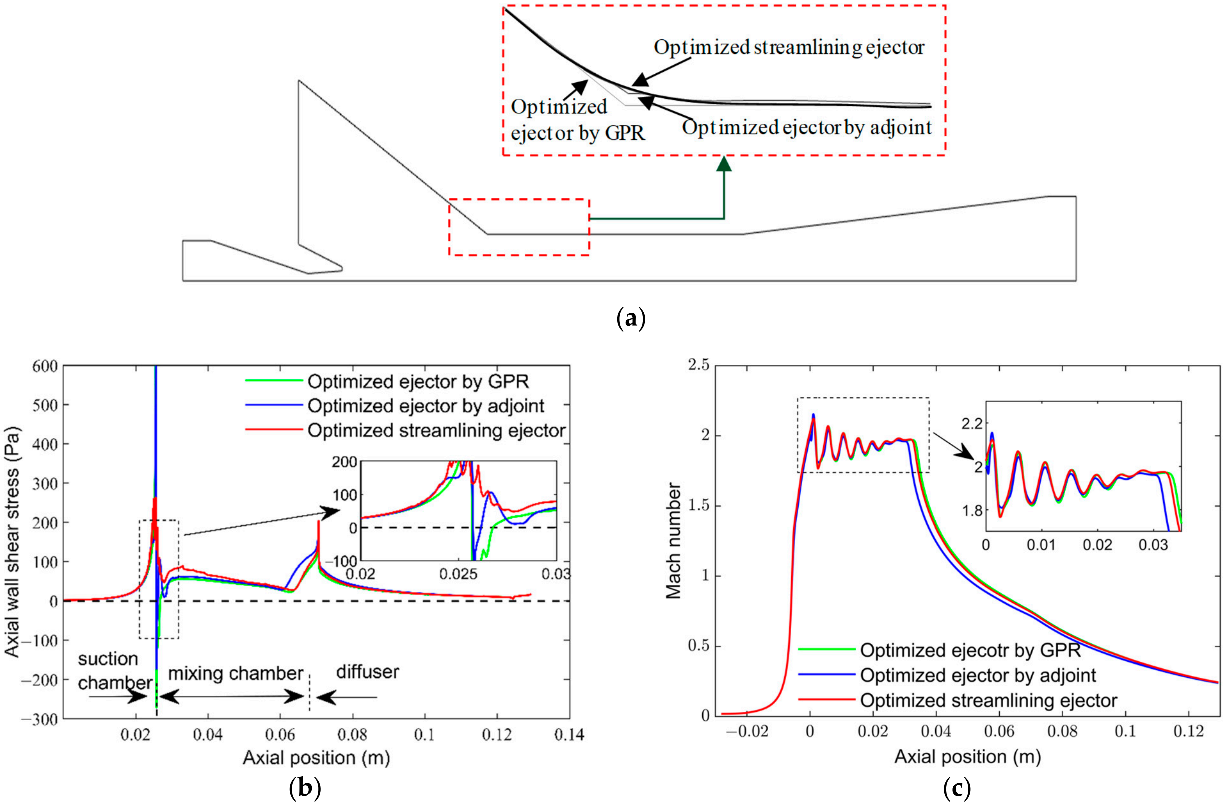

Figure 15. Comparisons of ejectors before and after local flow optimization using the adjoint method and streamlining modification. (**a**) Structure. (**b**) Axial wall shear stress. (**c**) Central Mach number.

Table 7. Comparisons of the performance before and after local flow optimization.

Optimized Ejector	ER	Min Axial Wall Shear Stress (Pa)	Max Axial Wall Shear Stress (Pa)	Vortex Scale (mm)
Optimized ejector via GPR	3.12	−271	936	0.98
Optimized ejector via adjoint	3.17	−172	735	0.33
Optimized streamlining ejector	3.18	53	263	0

Figure 16 verifies that the entrainment ratio of the ejector is improved via local flow optimization. The results of cases 1–9 facilitate a comparison of the ejector through optimized GPR and that optimized by streamlining modification. The results of cases 1–5 show that the entrainment ratio decreases with increases in the back pressure (pressure difference) of the ejector, and the entrainment ratio first increases and then decreases with increases in the back pressure. Under different back pressures, the ejector entrainment ratio increased by 2.77%—on average—after local flow optimization. The design point increased by 1.67%, and the maximum point increased by 3.99%. Case 5–9 show a comparison of the entrainment under different secondary inlet pressures. The results show that the entrainment gradually decreases with decreases in the secondary flow pressure. The increase rate of the entrainment ratio first increases and then decreases with decreases in the secondary flow pressure. The average increase rate is 2.34%. Although the increase in the entrainment ratio after local flow optimization is limited, it is clear that local flow optimization can promote the performance of the ejector. In comparison to the traditional optimization process, the optimization strategy proposed in this study can be used to improve the performance of the ejector.

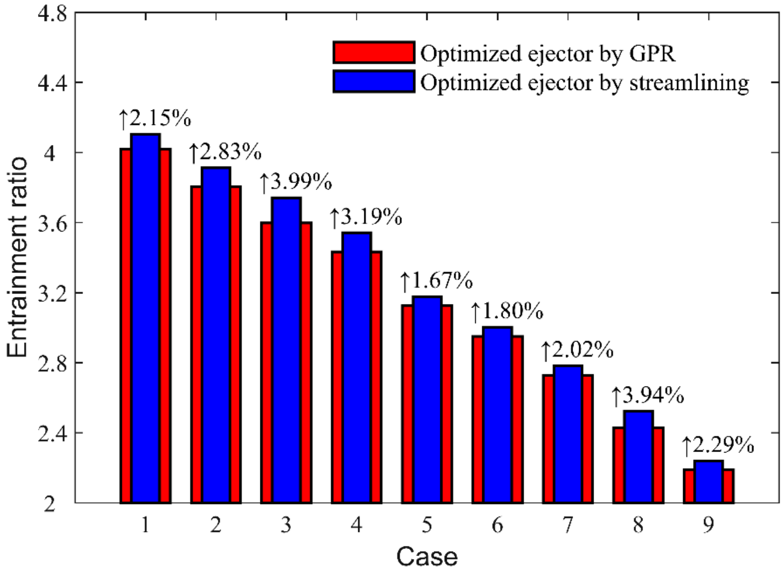

Figure 16. Entrainment ratios in different cases.

4. Conclusions

In this paper, a pulsed ejector is proposed for a PEMFC anode circulation system. It will help reduce hydrogen emissions during the PEMFC operating process, improve hydrogen utilization, and enhance energy sustainability. An optimization strategy for the pulsed ejector is also proposed, which provides a reference for its design. In this strategy, a CFD model was used to calculate the performance of the ejector, and a GPR model was trained. GWO is used to optimize the four key structural parameters globally, and the adjoint method was finally used to optimize the local flow field. Based on the results of global optimization and local flow optimization in this research, the following conclusions can be drawn:

(1) The back pressure affects the ejector performance by influencing the internal flow characteristics of the ejector. The increase in back pressure reduces the length of the shock train, resulting in the size of the separation vortex increasing with viscous boundaries, and the entrainment ratio decreases. When the secondary inlet pressure decreases, the entrainment ratio decreases.

(2) The multi-parameter interactions among the mixing chamber diameter, mixing chamber length, nozzle outlet position, and nozzle angle are significant. These major

structural parameters need to be globally optimized, and the entrainment ratio increases from 1.43 to 3.12 after global optimization using GPR and GWO.

(3) The junction regions between the suction chamber, mixing chamber, and nozzle region are highly sensitive to the entrainment ratio, which should be further optimized. Therefore, it is recommended to set a transition structure in this region when designing ejectors, using a small suction chamber angle or streamlined suction chamber.

(4) After local flow optimization using the adjoint method, the mixing uniformity of the two flows is promoted, and boundary layer separation is reduced. As a result, the minimum axial wall pressure increases from −271 Pa to 53 Pa, and the separation vortex at the entrance of the mixing chamber disappears. The entrainment ratio at the design point increases by 1.67%, reaching a maximum increase of 4% within a pulse cycle.

The strategy proposed in this paper can provide guidance for the optimization of PEMFC ejectors. For future work, the authors will focus on streamlined suction chamber optimization, transient studies on the pulsed ejector, and comprehensive performance research of the ejector-based PEMFC system, including modelling and experimental studies of the anode system in PEMFCs.

Author Contributions: Conceptualization, B.S.; Software, C.L.; Validation, C.L. and L.B.; Investigation, C.L.; Writing—original draft, C.L.; Writing—review and editing, B.S. and L.B.; Visualization, C.L. and B.S.; Supervision, B.S. All authors have read and agreed to the published version of the manuscript.

Funding: This research was supported by the Research and Development Project in Major Fields of Guangdong Province (Grant No. 2020B090920001) and the National Natural Science Foundation of China (Grant No. 5220061158).

Institutional Review Board Statement: Not applicable.

Informed Consent Statement: Not applicable.

Data Availability Statement: Data are available on request due to privacy.

Conflicts of Interest: The authors declare no conflicts of interest.

Nomenclature

A	Area (m^2)	Greek letters	
D	Diameter (m)	k	Turbulent kinetic energy
ER	Entrainment ratio	ω	Turbulent eddy frequency
F	Faraday's constant (C mol^{-1})	θ	Angle (°)
L	Length (m)	γ	Specific heat ratio
T	Temperature (K)	ρ	Density (kg m^3)
I	Current (A)	δ	Standard deviation
m	Mass flow rate (kg s^{-1})	Subscript	
M	Molar weight (kg mol^{-1})	p	Primary flow
Ma	Much number	s	Secondary flow
N	Number of single cell of PEMFC stack	c	Exit flow
P	Pressure (Pa)	t	Nozzle throat
R	Gas constant (J mol^{-1} K^{-1})	n	Nozzle
V	Velocity (m s^{-1})	y	Mixing chamber inlet
CFD	Computational fluid dynamics	v	Velocity distribution
SST	Shear stress transport	H_2	Hydrogen
GPR	Gaussian process regression	nd	Nozzle diffusion zone
GWO	Grey wolf optimization	m	Mixing chamber
PEMFC	Proton exchange membrane fuel cell	d	Diffusor

References

1. Jiao, K.; Li, X. Water transport in polymer electrolyte membrane fuel cells. *Prog. Energy Combust. Sci.* **2011**, *37*, 221–291. [CrossRef]
2. He, J.; Choe, S.-Y.; Hong, C.-O. Analysis and control of a hybrid fuel delivery system for a polymer electrolyte membrane fuel cell. *J. Power Source* **2008**, *185*, 973–984. [CrossRef]
3. Gu, P.; Xing, L.; Wang, Y.; Feng, J.; Peng, X. Transient flow field and performance analysis of a claw pump for FCVs. *Int. J. Hydrogen Energy* **2021**, *46*, 984–997. [CrossRef]
4. Jung, S.K.; Noh, Y.G.; Jeon, U.S. A Development of the Fuel Cell System That the Jet-Pump is Applied. In Proceedings of the ASME 2013 11th International Conference on Fuel Cell Science, Engineering and Technology collocated with the ASME 2013 Heat Transfer Summer Conference and the ASME 2013 7th International Conference on Energy Sustainability, Minneapolis, MN, USA, 14–19 July 2013.
5. Badami, M.; Mura, M. Leakage effects on the performance characteristics of a regenerative blower for the hydrogen recirculation of a PEM fuel cell. *Energy Convers. Manag.* **2012**, *55*, 20–25. [CrossRef]
6. Toghyani, S.; Afshari, E.; Baniasadi, E. A parametric comparison of three fuel recirculation system in the closed loop fuel supply system of PEM fuel cell. *Int. J. Hydrogen Energy* **2019**, *44*, 7518–7530. [CrossRef]
7. Liu, Z.; Liu, Z.; Jiao, K.; Yang, Z.; Zhou, X.; Du, Q. Numerical investigation of ejector transient characteristics for a 130-kW PEMFC system. *Int. J. Energy Res.* **2020**, *44*, 3697–3710. [CrossRef]
8. Genc, O.; Timurkutluk, B.; Toros, S. Performance evaluation of ejector with different secondary flow directions and geometric properties for solid oxide fuel cell applications. *J. Power Source* **2019**, *421*, 76–90. [CrossRef]
9. Yin, Y.; Fan, M.; Jiao, K.; Du, Q.; Qin, Y. Numerical investigation of an ejector for anode recirculation in proton exchange membrane fuel cell system. *Energy Convers. Manag.* **2016**, *126*, 1106–1117. [CrossRef]
10. Hou, M.; Chen, F.; Pei, Y. Optimization of geometric parameters of ejector for fuel cell system based on multi-objective optimization method. *Int. J. Green Energy* **2024**, *21*, 228–243. [CrossRef]
11. Han, J.; Besagni, G.; Mereu, R.; Inzoli, F.; Feng, J.; Peng, X. Performance investigation on the bypass ejector for a proton exchange membrane fuel cell system. *Appl. Therm. Eng.* **2024**, *241*, 122349. [CrossRef]
12. Yin, B.; Li, Z.; Dong, F.; Xu, S.; Ni, H. A novel dual-nozzle ejector for enhancement of hydrogen recirculation applied to proton exchange membrane fuel cell system. *J. Power Source* **2023**, *580*, 233444. [CrossRef]
13. Pei, P.; Ren, P.; Li, Y.; Wu, Z.; Chen, D.; Huang, S.; Jia, X. Numerical studies on wide-operating-range ejector based on anodic pressure drop characteristics in proton exchange membrane fuel cell system. *Appl. Energy* **2019**, *235*, 729–738. [CrossRef]
14. Wang, X.; Xu, S.; Xing, C. Numerical and experimental investigation on an ejector designed for an 80 kW polymer electrolyte membrane fuel cell stack. *J. Power Source* **2019**, *415*, 25–32. [CrossRef]
15. Maghsoodi, A.; Afshari, E.; Ahmadikia, H. Optimization of geometric parameters for design a high-performance ejector in the proton exchange membrane fuel cell system using artificial neural network and genetic algorithm. *Appl. Therm. Eng.* **2014**, *71*, 410–418. [CrossRef]
16. Bai, S.; Wang, L.; Wang, X. Optimization of ejector geometric parameters with hybrid artificial fish swarm algorithm for PEM fuel cell. In Proceedings of the 2017 Chinese Automation Congress (CAC), Jinan, China, 20–22 October 2017; pp. 3319–3322.
17. Zhang, X.; Wang, L.; Zhang, H.; Jia, L. Optimization of ejector structure for the PEMFC hydrogen recirculation system. In Proceedings of the 2020 Chinese Automation Congress (CAC), Shanghai, China, 6–8 November 2020; pp. 2954–2959.
18. Yang, Y.; Du, W.; Ma, T.; Lin, W.; Cong, M.; Yang, H.; Yu, Z. Numerical studies on ejector structure optimization and performance prediction based on a novel pressure drop model for proton exchange membrane fuel cell anode. *Int. J. Hydrogen Energy* **2020**, *45*, 23343–23352. [CrossRef]
19. Yan, J.; Wen, H. Multi-round optimization of an ejector with different mixing chamber geometries at various liquid volume fractions of inlet fluids. *Appl. Therm. Eng.* **2022**, *200*, 117709. [CrossRef]
20. Wu, Y.; Zhao, H.; Zhang, C.; Wang, L.; Han, J. Optimization analysis of structure parameters of steam ejector based on CFD and orthogonal test. *Energy* **2018**, *151*, 79–93. [CrossRef]
21. Amin, A.; Elbadawy, I.; Elgendy, E.; Fatouh, M. Effect of geometrical factors interactions on design optimization process of a natural gas ejector. *Adv. Mech. Eng.* **2019**, *11*, 168781401988036. [CrossRef]
22. Bian, J.; Zhang, Y.; Liu, Y.; Gong, L.; Cao, X. Structural optimization of hydrogen recirculation ejector for proton exchange membrane fuel cells considering the boundary layer separation effect. *J. Clean. Prod.* **2023**, *397*, 136535. [CrossRef]
23. Ringstad, K.E.; Banasiak, K.; Ervik, Å.; Hafner, A. Machine learning and CFD for mapping and optimization of CO_2 ejectors. *Appl. Therm. Eng.* **2021**, *199*, 117604. [CrossRef]
24. Dadvar, M.; Afshari, E. Analysis of design parameters in anodic recirculation system based on ejector technology for PEM fuel cells: A new approach in designing. *Int. J. Hydrogen. Energy* **2014**, *39*, 12061–12073. [CrossRef]
25. Zhu, Y.; Li, Y. New theoretical model for convergent nozzle ejector in the proton exchange membrane fuel cell system. *J. Power Source* **2009**, *191*, 510–519. [CrossRef]
26. Huang, Y.; Jiang, P.; Zhu, Y. Shape optimization and flow irreversibility mechanism analysis of normal temperature, high temperature and wet stream ejectors. *Appl. Therm. Eng.* **2024**, *242*, 122468. [CrossRef]
27. Brunner, D.A.; Marcks, S.; Bajpai, M.; Prasad, A.K.; Advani, S.G. Design and characterization of an electronically controlled variable flow rate ejector for fuel cell applications. *Int. J. Hydrogen Energy* **2012**, *37*, 4457–4466. [CrossRef]

28. Song, Y.; Wang, X.; Wang, L.; Pan, F.; Chen, W.; Xi, F. A twin-nozzle ejector for hydrogen recirculation in wide power operation of polymer electrolyte membrane fuel cell system. *Appl. Energy* **2021**, *300*, 117442. [CrossRef]
29. Du, Z.; Liu, Q.; Wang, X.; Wang, L. Performance investigation on a coaxial-nozzle ejector for PEMFC hydrogen recirculation system. *Int. J. Hydrogen Energy* **2021**, *46*, 38026–38039. [CrossRef]
30. Xue, H.; Wang, L.; Zhang, H.; Jia, L.; Ren, J. Design and investigation of multi-nozzle ejector for PEMFC hydrogen recirculation. *Int. J. Hydrogen Energy* **2020**, *45*, 14500–14516. [CrossRef]
31. Han, J.; Feng, J.; Hou, T.; Peng, X. Performance investigation of a multi-nozzle ejector for proton exchange membrane fuel cell system. *Int. J. Energy Res.* **2021**, *45*, 3031–3048. [CrossRef]
32. Yu, M.; Wang, C.; Wang, L.; Wang, X.; Li, D. Auxiliary-ejector-based hydrogen recirculation system to broaden PEMFC operating range. *Int. J. Hydrogen Energy* **2024**, *57*, 515–529. [CrossRef]
33. Kim, M.J.; Lee, W.Y.; Kim, C.-S. Development of the Variable Multi-ejector for a Mini-bus PEMFC System. *ECS Trans.* **2007**, *5*, 773–780. [CrossRef]
34. Huang, P.-H.; Kuo, J.-K.; Wu, C.-B. Design and evaluation of dual passive hydrogen recovery subsystem for 10 kW PEMFC. *Int. J. Hydrogen Energy* **2023**, *54*, 483–491. [CrossRef]
35. Hwang, J.-J. Passive hydrogen recovery schemes using a vacuum ejector in a proton exchange membrane fuel cell system. *J. Power Source* **2014**, *247*, 256–263. [CrossRef]
36. Singer, G.; Gappmayer, G.; Macherhammer, M.; Pertl, P.; Trattner, A. A development toolchain for a pulsed injector-ejector unit for PEM fuel cell applications. *Int. J. Hydrogen Energy* **2022**, *47*, 23818–23832. [CrossRef]
37. Nikiforow, K.; Koski, P.; Karimäki, H.; Ihonen, J.; Alopaeus, V. Designing a hydrogen gas ejector for 5 kW stationary PEMFC system—CFD-modeling and experimental validation. *Int. J. Hydrogen Energy* **2016**, *41*, 14952–14970. [CrossRef]
38. Gupta, S.; Deep, K. A memory-based Grey Wolf Optimizer for global optimization tasks. *Appl. Soft Comput.* **2020**, *93*, 106367. [CrossRef]
39. Besagni, G.; Inzoli, F. Computational fluid-dynamics modeling of supersonic ejectors: Screening of turbulence modeling approaches. *Appl. Therm. Eng.* **2017**, *117*, 122–144. [CrossRef]
40. Hosseinzadeh, E.; Rokni, M.; Jabbari, M.; Mortensen, H. Numerical analysis of transport phenomena for designing of ejector in PEM forklift system. *Int. J. Hydrogen Energy* **2014**, *39*, 6664–6674. [CrossRef]
41. Chong, D.; Hu, M.; Chen, W.; Wang, J.; Liu, J.; Yan, J. Experimental and numerical analysis of supersonic air ejector. *Appl. Energy* **2014**, *130*, 679–684. [CrossRef]
42. Li, C.; Sun, B.; Luo, Q. Effect of Structural Parameters and Operational Characteristic Analysis on Ejector Used in Proton Exchange Membrane Fuel Cell. *Sustainability* **2022**, *14*, 9205. [CrossRef]